Influence of a Temperature Driven Structural Phase Transition on the Ionic Conductivity of $Na_6Mn(SO_4)_4$ Vanthoffite System

Madhulika Mazumder[†] and Swapan K Pati[*,†,‡]

†*New Chemistry Unit, School of Advanced Materials Science (SAMat), Jawaharlal Nehru Centre for Advanced Scientific Research (JNCASR), Bangalore 560064, India*

‡*Theoretical Sciences Unit, School of Advanced Materials Science (SAMat), Jawaharlal Nehru Centre for Advanced Scientific Research (JNCASR), Bangalore 560064, India*

E-mail: swapan.jnc@gmail.com

Abstract

Sodium Ion Batteries have emerged as practicable successors of the Li-ion battery technology with respect to performance, availability and safety. However, to address the ever-growing demand of improving energy density and capacity, it is important to invest into the research of materials that can serve as efficient battery components and ensure high operational voltages along with long term stability. In this regard,the design of cathode systems calls for special attention as they govern the output voltage of the cell. Polyanionic sulfate materials are known for their high cathodic efficiency owing to their energy densities that arise from electronegativity of sulfate anions. The Vanthoffite class of compounds, with their open framework skeletons, have been explored experimentally as good ionic conductors, which show a temperature dependent ionic conductivity. A superionic phase transition was found in the Mn based system at 445 °C, which was is reversible. Our theoretical calculations provide a mechanistic

insight into this phase transition, which is due to the cumulative effect of the changes in the local topology. Our analysis also establishes $Na_6Mn(SO_4)_4$ to be an efficient cathode material for sodium ion batteries.

Introduction

Over the past few decades, the desire to enhance energy storage technology has created numerous obstacles for the design and scalability of battery components, particularly the electrodes and electrolytes. While lithium ion batteries (LIBs), with their high energy density and working potential, have been a huge success in the field of portable electronics, large-scale applications like grid storage and plug-in hybrid vehicles (PHEVs) depend on material cost and abundance in addition to ideal energy densities. Due to the scarcity of lithium and its high price, there are certain concerns about the use of lithium-ion batteries in large-scale energy storage systems. Sodium-ion batteries, despite having a lower energy density than lithium-ion batteries, can be a cheaper alternative fit for large scale usage.[1,2] The diffusion of Na^+ to insert into or withdraw from the host material is constrained by its bigger size (1.02 Å) compared to Li^+ (0.76 Å), which affects the overall kinetics and electrode integrity.[3,4]

The structural stability of electrode materials greatly affects cycling characteristics of the cells. Many cathode materials are prone to rapid capacity fade by the irreversible structural alterations brought about by the cycles of sodiation and desodiation processes.[5] Tuning cationic as well as anionic units have been proved to enhance the efficiency and electrochemical performance, altering the chemical properties at the atomistic level. Recently, many cathode materials, such as, metal oxides,[6,7] prussian blue compounds,[8–10] polyanions[11,12] and organic materials[13] have been applied in SIBs.

Polyanionic compounds are characterized by an anionic structural unit $(XO_m)^n$ (X = P, S, As, W, and others) with tetrahedral or octahedral structural units.[14] Due to the diversity and stability of the construction, the impressive inductive effect of the anions, as well as high operating potentials and remarkable cycling stability, these systems can be

regarded as potential cathode materials. Notable progress has been made in phosphates,[15–17] fluorophosphates[18? ,19] pyrophosphates,[20,21] and sulfates.[22–24]

Owing to the high electronegativity of the $(SO_4)_2^-$ group, higher redox voltages of $M^{n^+/n+1^+}$ can be achieved, as explained by the inductive effect. Moreover, the open three-dimensional skeleton of PSM (Polysulfate materials) provides stable routes for ionic and electronic transfer with minimal volumetric fluctuations. This makes the sulfate based systems attractive for cathodic application. $NaFeSO_4F$ was one of the first sulfate based systems found to have a redox plateau at 3.6V, albeit with poor electrochemical reversibility.[25] This was followed by extensive experimental and theoretical research on PSMs, by tuning a range of cationic as well as polyanionic centres.

One class of such PSM compounds, vanthoffites are found as minerals in oceanic salt deposits. They have a structural formula of $Na_6M(SO_4)_4$ (M=Mn, Co, Ni, Fe, Mg). It is expected that due to the high content of Na ions together with the facile coordination around Na ions, would allow easy migration of Na ions within the structure. Interestingly, Row et al. observed superionic behaviour (10^{-2} S.cm^{-1}) at around 445° C with low ion migration barriers.[26] The superionic behaviour is possibly a result of a temperature-driven structural phase transition, which is not uncommon in this class of materials. Also, it was found to be reversible. This can further be utilized in the design of a possible switchable superionic material and can be tested in the sodium-ion battery.[27]

We consider the $Na_6M(SO_4)_4$ crystal structures and performed an initial scan for the energy stability with 3d transition metal cations, M = Mn, Co, Ni and Fe. After carefully considering the energy stability, the M= Mn based system was found to have the lowest electronic energy and was thus selected for further studies.

Computational Methods

First Principles Density Functional Theory (DFT) calculations were performed in Vienna Ab-Initio Simulation Package (VASP).[28–31] Perdew-Burke-Ernzerhorf (PBE)[33] functional under Generalized Gradient Approximation (GGA)[32] was used to treat the exchange and correlation effects. Optimised lattice parameters obtained from PBE functional were in line with experimental reports, thus PBE was chosen for further calculations. Projector Augmented Wave (PAW)[35,36] pseudopotentials were used to approximate interactions between nucleus and core electrons. Kinetic Energy cutoff of 520 eV was maintained for PW expansion. A Hubbard U correction ($U_{Mn} = 3.9eV$),[37–39] was taken to treat the effects of electronic correlations. Brillouin Zone integration was performed with $6 \times 6 \times 1$ Monkhorst-Pack grids. The geometry was optimized by conjugate-gradient algorithm with a threshold of 10^{-2} eV/atom for interatomic forces. A $2 \times 1 \times 1$ supercell was used for calculations, containing 2 formula units of $Na_6Mn(SO_4)_4$.

Climbing Image-Nudged Elastic Band (CI-NEB) was employed to find the Minimum Energy Pathway as well as the activation barrier for Na hopping.[40] *Ab-Initio* Molecular Dynamics (AIMD) simulations were carried out to study Na diffusion dynamics. The atomic trajectories were calculated using an NPT ensemble with a Langevin Thermostat, until the systems were equilibrated.[42] Simulations were then run for a total of 80ps with a 2fs time-step for all simulations, for temperatures ranging from 300 to 1000 K, to observe the displacement of Na ions. The ionic conductivities were obtained at varying temperatures, from the calculated diffusion coefficients, using the Nernst-Einstein relation. The total displacement as a function of the time taken for the diffusion process, is a summation of individual ionic displacements $\overrightarrow{r}$, and is described by $\overrightarrow{R}(t) = \Sigma_i^N \overrightarrow{r}_i(t)$

According to the Einstein relation, the chemical diffusivity (D) can be expressed as:

$$D = \frac{1}{2d} \lim_{t \to \infty} \frac{\left\langle \frac{1}{N} \overrightarrow{R}(t)^2 \right\rangle}{t} \tag{1}$$

where d is the dimensionality of diffusion channels (i.e. d=3 for 3-dimensional channels); a statistical/ensemble average of the total displacement of all the Na ions, $\overrightarrow{R}(t)$ is taken since ionic migration is a completely stochastic phenomenon.

The diffusion coefficient D can be related to the Ionic Conductivity, σ by the Nernst-Einstein equation as follows :

$$\sigma(T) = \frac{Ne^2}{V \times k_B T} \times D(T) \tag{2}$$

where, N is the number of Na ions, V is the total volume of the cell considered for simulation, e is the electronic charge of the mobile species, k_B is Boltzmann's constant, ($8.617 \times 10^{-5} eVK^{-1}$) and T is the temperature in Kelvin scale. It is understandable that diffusivity D varies with temperature and will have a direct effect on the ionic conductivity, σ, which in itself, is inversely proportional to temperature.

Results and discussion

Crystal Structure Analysis

$Na_6M(SO_4)_4$ crystallises in a monoclinic structure (Space group : $P2_1/c$). The optimized lattice parameters are tabulated in Table 1. It is characterized by rows of MO_6 octahedra along the [001] direction, corner-shared with SO_4 tetrahedra. The zig-zag intersecting chain of $MO_6 - SO_4 - MO_6$ units is continuous along the b-axis, and cross-linked by the sulphate tetrahedra. The Na ions reside in the interstitial sites of this 2D network of $MO_6 - SO_4 - NaO_6 - MO_6$ units. There exists 2 types of A-B-A-B layers along the b and c axes, with respect to the Na arrangement. The Layer A consists of edge shared NaO_7 units, while the Layer B has a $NaO_6 - SO_4 - NaO_7$ network. The M centre is symmetrically unique (Wyckoff : $2a$), but there are 2 distinguishable Na environments with different oxygen coordination. The Na(1) sites have 6-fold coordination, while the Na(2) site has 5-fold

coordination of oxygen atoms. The $(SO_4)_2$ groups display a 3D network of slightly distorted tetrahedra. Oxygen atoms connect all the polyhedra in the lattice.

Table 1: Optimized lattice parameters (reported in Materials Project mp-1210321) and Bond distances

a (Å)	c(Å)	β	Mn-O(Å)	Na-O (Å)
8.421(8.420)	10.011(10.010)	113.696	2.16	2.46, 2.40

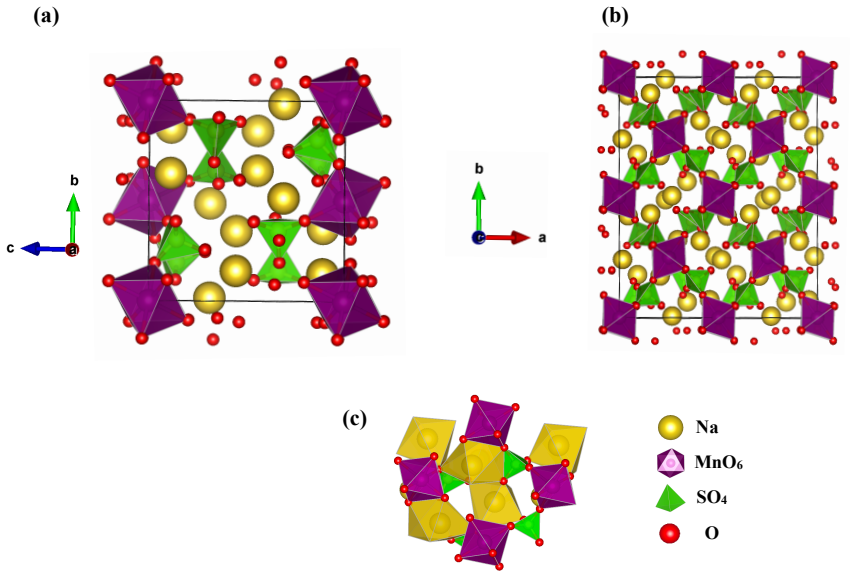

Figure 1: Crystal Structure of Vanthoffite $Na_6M(SO_4)_4$ system viewed across a) *bc* and (b) *ab* planes. (c) Na coordination and polyhedral connectivity

Thermodynamic Stability

To predict the thermodynamic stability of $Na_6M(SO_4)_4$, we computed the enthalpy of formation from stable synthetic precursors, $Na_2(SO_4)$ and $MnSO_4$) . This revealed a more negative formation enthalpy for our target compound, thus indicating the feasibility of synthesizing it in ambient conditions.

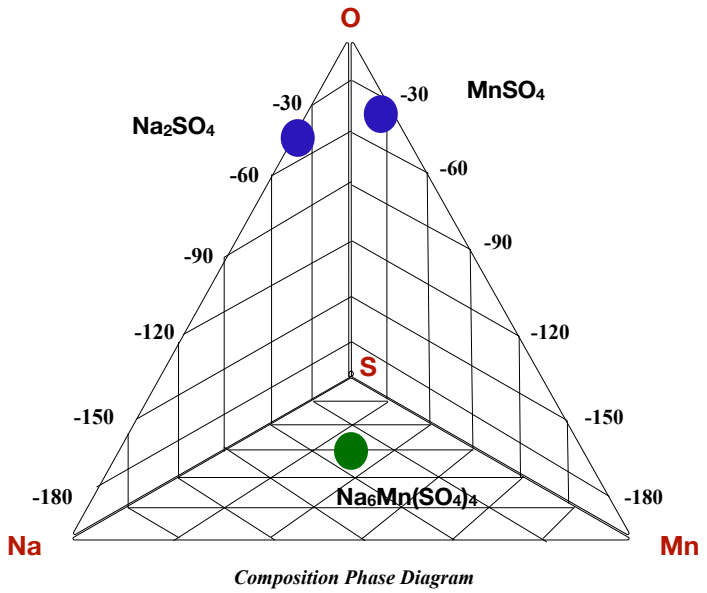

Figure 2: Compositional Analysis from Synthetic Precursors

Desodiation Profile

The thermodynamic stability of intermediate compositions encountered upon desodiation of the system was probed by constructing the convex hull plot of formation energy per formula unit varied as a function of composition x of Na. The enthalpy of formation was calculated using the following equation :

$$\Delta H_f = E_i - \frac{x}{6} \times (E_{Na_6M(SO_4)_4}) - \frac{(6-x)}{6} \times (E_{M(SO_4)_4}) \tag{3}$$

where, x is the Na content, E_i is the electronic energy of the intermediate species after x amount of Na removal (desodiation).

From the convex hull plot, Na ordering is observed for all the compositions upto $x = 1$, which suggests that the deep Na extraction is feasible at a higher voltage window above 4.5 V. The minima of the convex hull is found at $x = 3$, but a solid solution mechanism is expected to be followed throughout the desodiation process.

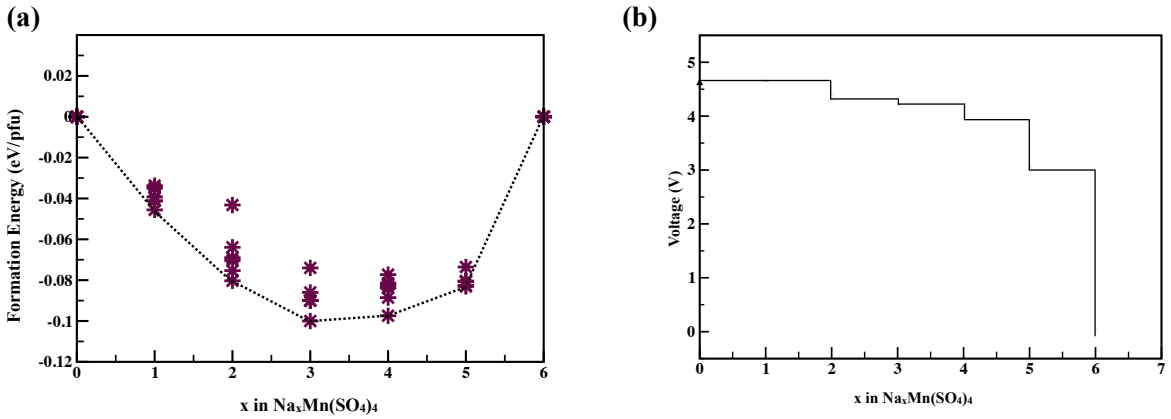

Figure 3: a) Convex Hull Plot showing ordered phases during desodiation and b) corresponding voltages

Evolution of Structure with temperature

As shown by Sharma et al.,[26] the superionic conductivity is triggered at elevated temperatures above 445° C, which is the temperature of phase transition from orthorhombic to monoclinic phase. Our AIMD simulations suggest that both the lattice parameters and the topology of Mn^{2+} centres undergo a change above 718 K. The Mn^{2+} octahedra is seen to undergo a distortion at 600 K arising from the shortening of Mn-O bonds. At 718 K (i.e. 445° C), the Mn^{2+} ions begin to acquire a 4-coordinate tetrahedral geometry, with further reduction of Mn-O bond distances and elongation of Na-O bonds. [Table 2]. This improves the Na ionic mobility as observed from the computed diffusion coefficients and ionic mobility. The ionic conductivity at 718 K was found to be impressively high - 10^{-2}Scm^{-1} and linearly increased with temperature, thus confirming the superionic behaviour of this system at high temperature. The evolution of local structure can be visualised in [Fig. 4].

Table 2: Bond distances at different temperatures after 50 ps AIMD simulations

Temperature (K) (° C)	Mn-O(Å)	Na-O(Å)
300 (27)	2.16	2.46, 2.58
600 (327)	1.78,1.84	2.42,2.55
718 (445)	1.71, 1.79	2.52, 2.59
900 (627)	1.71, 1.80	2.42, 2.54

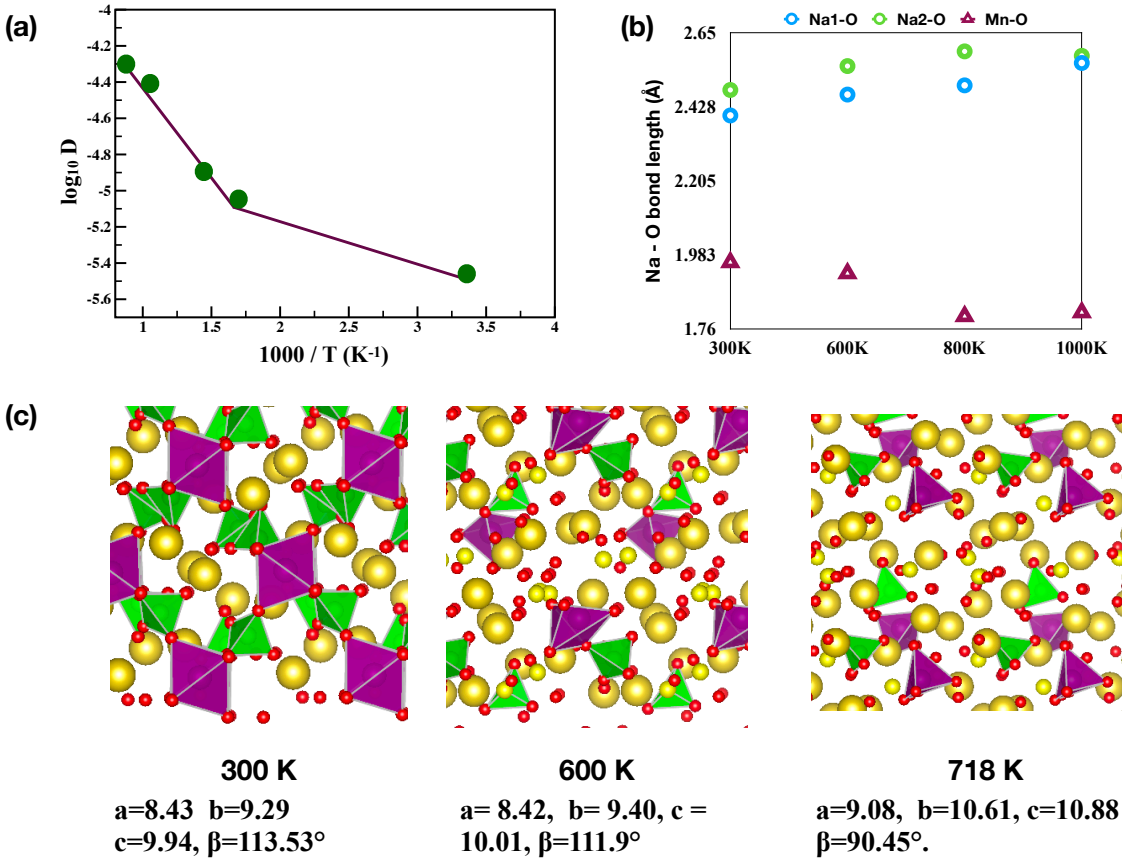

Figure 4: (a) Superionic behaviour evident from log D as a function of inverse of temperature, (b) Evolution of Na(1)-O, Na(2)-O and Mn-O bond lengths, (c) AIMD Snapshots showing change in local topology leading to conversion of Monoclinic to Orthorhombic lattice

To understand the change in Mn^{2+} local environment, we computed the electronic structures of the geometries obtained from AIMD simulations at temperatures below, above and at the transition temperature 718 K. As seen in [Fig. 5], the computed projected density of states can be characterized by non-bonding t_{2g} orbitals and bonding e_g orbitals populating the valence bands below the Fermi level. The $3d_{z^2} and 3d_{x^2-y^2}$ of Mn orbitals are hybridized with 2p and 3p of O and S orbitals respectively, to form the bonding σ states. The anti-bonding σ^* states are majorly comprised by the e_{g^*} states of the Mn^{2+}. AIMD simulations were carried out up to 80ps at constant temperatures, at T=718K and at mention T values. The projected density of states (PDOS) calculations were then performed on the structures obtained from the AIMD simulations. At 718 K and above, the Mn crystal field splitting

is found to be quite different. It was observed that the Mn $3d_{xy}, 3d_{yz}, 3d_{xz}$ orbitals now populate the antibonding σ^* states, whereas the $3d_{x^2-y^2}, 3d_{z^2}$ orbitals lie below the Fermi level comprising the valence bands. This corresponds to an Mn^0_d state that is formed upon in which the Mn prefers to acquire a tetrahedral coordination. It is speculated that the superionic phase transition involving Na^+ diffusion is accompanied by a change in the crystal field of Mn centres, which also leads to a deformation of the lattice to an orthorhombic ($Pmmm$) phase.

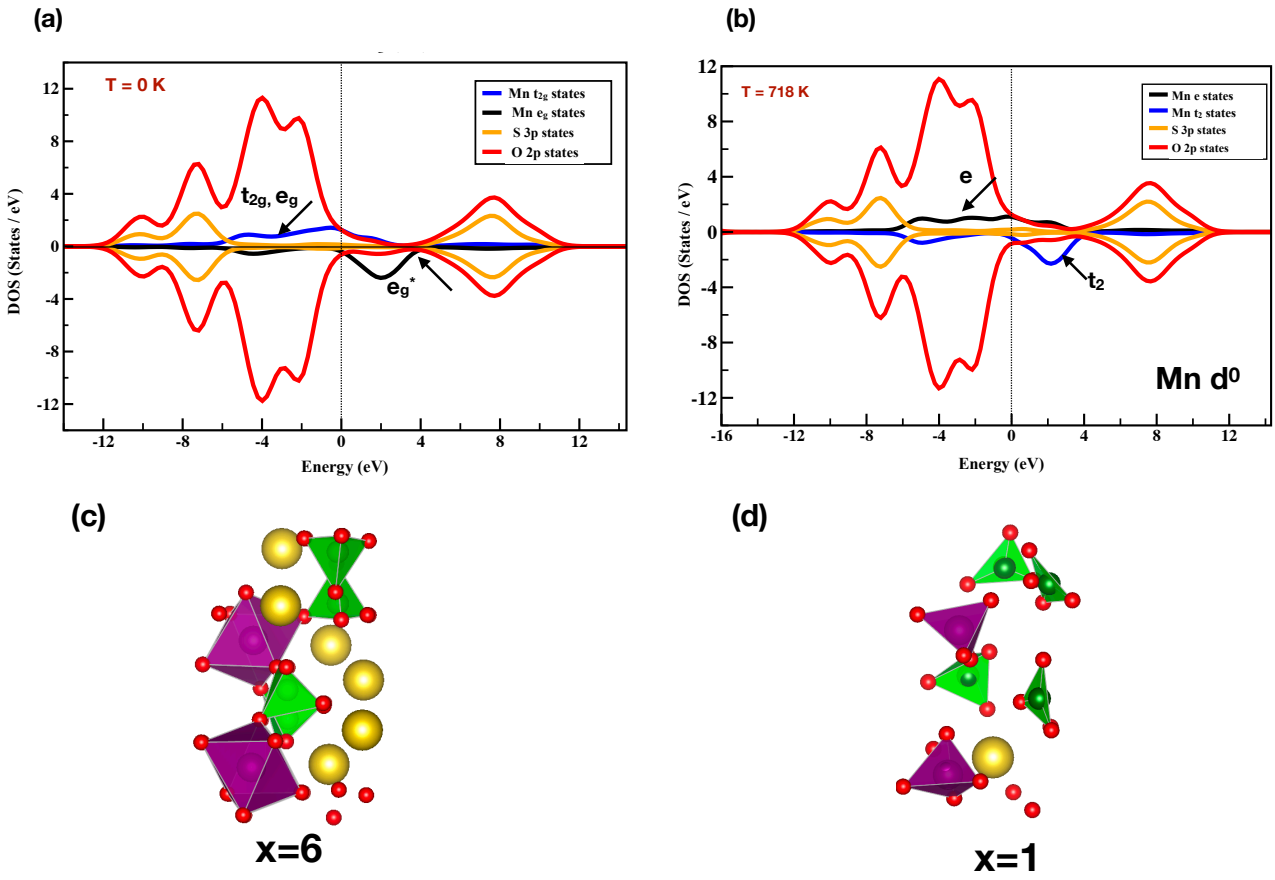

Figure 5: Evolution of electronic structure with Temperature. Projected DOS for a) 0 K geometry and b) 718 K geometry (c) Evolution of Mn coordination

CI-NEB calculations revealed low Na migration barrier of 0.24 eV, and the Minimum Energy Pathway was found to lie along [010] direction.

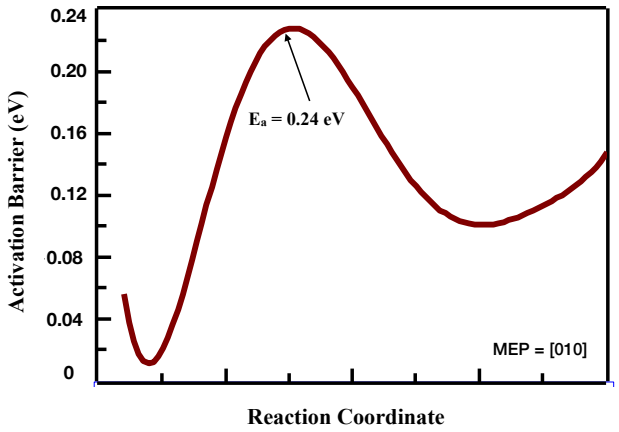

Figure 6: CI-NEB computed Activation Barrier

Conclusion

In summary, the vanthoffite class of materials was explored for cathodic properties. The Mn analog was found to be the most stable member among the 3d Transition Metal cations. The ionic conductivity was found to be significantly high, as is generally seen in superionic conductors. The superionic behaviour was explained by a temperature driven structural phase transition, in which, the octahedral to tetrahedral transition of the Mn centres was responsible for causing a lattice distortion and in turn facilitated fast Na ion diffusion.

Conflicts of interest

The authors declare no conflicts of interest.

Acknowledgement

MM acknowledges JNCASR for the Fellowship and SKP acknowledges JC Bose Fellowship, SERB, DST, Govt. of India for financial support. Authors thank NSM-ParamYukti and CCMS for computational facilities.

References

(1) K. Kaliyappan, T. Or, Y. P. Deng, Y. Hu, Z. Bai and Z. Chen, *Adv. Funct. Mater.*, 2020, **30**, 1910251.

(2) L. Mu, S. Xu, Y. Li, Y. S. Hu, H. Li, L. Chen and X. Huang, *Adv. Mater.*, 2015, **27**, 6928-6933.

(3) J. Xiao, F. Zhang, K. Tang, X. Li, D. Wang, Y. Wang, H. Liu, M. Wu and G. Wang, *ACS Cent. Sci.*, 2019, **5**, 1937-1945.

(4) X. Guo, X. Xie, S. Choi, Y. Zhao, H. Liu, C. Wang, S. Chang and G. Wang, *J. Mater. Chem. A*, 2017, **5**, 12445-12452.

(5) K. Tang, J. Xiao, X. Li, D. Wang, M. Long, J. Chen, H. Gao, W. Chen, C. Liu and H. Liu, *Front. Chem.*, 2020, **8**, 595972.

(6) L. Liu, X. Li, S. H. Bo, Y. Wang, H. Chen, N. Twu, D. Wu and G. Ceder, *Adv. Energy Mater.*, 2015, **5**, 1500944.

(7) . K. Luo, M. R. Roberts, R. Hao, N. Guerrini, D. M. Pickup, Y. S. Liu, K. Edstrom, J. Guo, A. V. Chadwick, L. C. Duda and P. G. Bruce, *Nat. Chem.*, 2016, **8**, 684-691.

(8) Y. Tang, W. Li, P. Feng, M. Zhou, K. Wang, Y. Wang, K. Zaghib and K. Jiang, *Adv. Funct. Mater.*, 2020, **30**, 1908754.

(9) Y. Lyu, Y. Liu, Z. E. Yu, N. Su, Y. Liu, W. Li, Q. Li, B. Guo and B. Liu, *Sustainable Mater. Technol.,*, 2019, 21, e00098.

(10) A. Mukherjee, T. Sharabani, I. Perelshtein and M. Noked, *Batteries Supercaps*, 2019, **3**, 52-55.

(11) Y. Fang, L. Xiao, X. Ai , Y. Cao and H. Yang, *Adv. Mater.*, 2015, **27**, 5895-5900.

(12) Y. Zhao, X. Gao, H. Gao, H. Jin and J. B. Goodenough, *Adv. Funct. Mater.*, 2020, **30**, 1908680.

(13) H. Lyu, C. J. Jafta, I. Popovs, H. M. Meyer, J. A. Hachtel, J. Huang, B. G. Sumpter, S. Dai and X. G. Sun, *J. Mater. Chem. A*, 2019, **7**, 17888-17895.

(14) C. Masquelier, and L. Croguennec, *Chem. Rev.*, 2013, **113**, 65526591.

(15) K. Saravanan, C. W. Mason, A. Rudola, K. H. Wong and P. Balaya, *Adv. Energy Mater.*, 2013, **3**, 444-450.

(16) R. Rajagopalan, B. Chen, Z. Zhang, X. L. Wu, Y. Du, Y. Huang, B. Li, Y. Zong, J. Wang, G. H. Nam, M. Sindoro, S. X. Dou , H. K. Liu and H. Zhang, *Adv. Mater.*, 2017, **29**, 1605694.

(17) F. Xiong, Q. An, L. Xia, Y. Zhao, L. Mai, H. Tao and Y. Yue, *Nano Energy*, 2019, **57**, 608-615.

fluorophosphate1 B. L. Ellis, W. R. Makahnouk, Y. Makimura, K. Toghill and L. F. Nazar, *Nat. Mater.*, 2007, **6**, 749-753.

(18) G. Yan, S. Mariyappan, G. Rousse, Q. Jacquet, M. Deschamps, R. David, B. Mirvaux, J. W. Freeland and J. M. Tarascon, *Nat. Commun.*, 2019, **10**, 585.

(19) Y. U. Park, D. H. Seo, H. Kim, J. Kim, S. Lee, B. Kim and K. Kang, *Adv. Funct. Mater.*, 2014, **24**, 4603-4614.

(20) M. Chen, L. Chen, Z. Hu, Q. Liu, B. Zhang, Y. Hu, Q. Gu, J. L. Wang, L. Z. Wang, X. Guo, S. L. Chou and S. X. Dou, *Adv. Mater.*, 2017, **29**, 1605535.

(21) H. Kim, I. Park, S. Lee, H. Kim, K. Y. Park, Y. U. Park, H. Kim, J. Kim, H. D. Lim, W. S. Yoon and K. Kang, *Chem. Mater.*, 2013, **25**, 3614-3622.

(22) P. Barpanda, G. Oyama, C. D. Ling and A. Yamada, *Chem. Mater.*, 2014, **26**, 1297-1299.

(23) W. Pan, W. Guan, S. Liu, B. B. Xu, C. Liang, H. Pan, M. Yan and Y. Jiang, *J. Mater. Chem. A*, 2012, **7**, 13197-13204.

(24) X. Xiang, K. Zhang and J. Chen, *Adv. Mater.*, 2015, **27**, 5343-5364.

(25) P. Barpanda, J. Chotard, N. Recham, C. Delacourt, M. Ati, L. Dupont, M. Armand and J. Tarascon, *Inorg. Chem.*, 2010, **49**, 7401–7413.

(26) V. Sharma, D. Swain, and T. N. Guru Row, *Inorg. Chem.*, 2017, **56**, 6048-6051.

(27) A. Souamti, M. Kahlaoui, R. Fezai, A. DiegoLozano-Gorrínd, D. Ben, H. Chehimi, *Materials Science and Engineering: B*, 2019, **244**, 56-64.

(28) Kresse, G.; Hafner, J. Ab initio Molecular Dynamics for Liquid Metals *Phys. Rev. B: Condens. Matter Mater. Phys.* 1993, **47**, 558-561.

(29) G. Kresse and J. Furthmüller, *Comput. Mater. Sci.*, 1996, **6**, 15-50.

(30) G. Kresse and J. Hafner, *Phys. Rev. B: Condens. Matter Mater. Phys.*, 1994, **49**, 14251-14269.

(31) G. Kresse and J. Furthmüller, *Phys. Rev. B: Condens. Matter Mater. Phys.*, 1996, **54**, 11169-11186.

(32) A. Ruzsinszky, G. I. Csonka. O. A. Vydrov, G. E. Scuseria, L. A. Constantin, X. Zhou and K. Burke, *Phys. Rev. Lett.*, 2008, **100**, 136406.

(33) J. P. Perdew, K. Burke and M. Ernzerhof, *Phys. Rev. Lett.*, 1996, **77**, 3865-3868.

(34) J. P. Perdew, J. A. Chevary, S. H. Vosko, K. A. Jackson, M. R. Pederson, D. J. Singh and C. Fiolhais, *Phys. Rev. B*, 1992, **23**(45), 6671.

(35) G. Kresse, and D. Joubert, *Phys. Rev. B: Condens. Matter Mater. Phys.*, 1999, **59**, 1758-1775.

(36) P. E. Blöchl, *Phys. Rev. B: Condens. Matter Mater. Phys.*, 1994, **50**, 17953-17979.

(37) S. L. Dudarev, G. A. Botton, S. Y. Savrasov, C. J. Humphreys and A. P. Sutton, *Phys. Rev. B: Condens. Matter Mater. Phys.*, 1998, **57**, 1505-1509.

(38) S. L. Dudarev, G. A. Botton, S. Y. Savrasov, Z. Szotek, W. M. Temmerman and A. P. Sutton, *Phys. Status Solidi A*, 1998, **166**, 429-443.

(39) A. Jain, G. Hautier, C. J. Moore, S. P. Ong, C. C. Fischer, T. Mueller, K. A. Persson and G. Ceder, *Computational Materials Science*, 2011, **50**, 2295–2310.

(40) G. Henkelman, B. P. Uberuaga and H. Jónsson, *J. Chem. Phys.*, 2000, **113**, 9901-9904.

(41) D. J. Evans and B. L. Holian, *J. Chem. Phys.* 1985, **83**, 4069-4074.

(42) M. Allen and D. Tildesley, *Computer Simulation of Liquids*, Clarendon Press, 1989